Computational Materials Science 245 (2024) 113292

Contents lists available at ScienceDirect

Computational Materials Science

journal homepage: www.elsevier.com/locate/commatsci

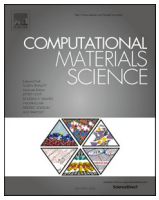

Full Length Article

Computational approach to modeling electronic properties of titanium oxynitride systems

Abiodun A. Odusanya [a], Dhananjay Kumar [a], J. David Schall [a,*], Justin Mayer [b], Ridwan Sakidja [c]

[a] Department of Mechanical Engineering, North Carolina A&T State University, Greensboro, NC 27411, United States
[b] University of California Santa Barbara, Santa Barbara, CA 93106, United States
[c] Missouri State University, Springfield, MO 65897, United States

ARTICLE INFO

Keywords:
Titanium oxynitride
Bandgap
On-lattice sampling
Trap states

ABSTRACT

The study presents the use of a novel on-lattice sampling approach to generate titanium oxynitride (TiN_xO_y) structures with potential applications in photovoltaic and water splitting. This approach presents a simple route to overcome challenges with structure-generating tools like Cluster Approach to Statistical Mechanics (CASM), and Ab initio Random Structure Search (AIRSS), CASM faces difficulty in generating ternary structures with large unit cells. With AIRSS, there is an increase in probability of sampling amorphous sample spaces with increased number of atoms in the unit cell. Here an on-lattice sampling approach was used to model the electronic structure of TiN_xO_y as a function of composition. We present results for Ti_2N_2O, $Ti_5N_4O_4$ and $Ti_7N_4O_8$, with 33 %, 50 % and 67 % N replaced by O via substitution relative to titanium nitride (TiN), respectively. Koopmans theorem was used correct the Kohn-Sham Density Functional Theory (KS-DFT) bandgaps with corresponding values of 2.68 eV, 3.03 eV, and 3.65 eV for 33, 50 and 67 % O doping respectively. The projected density of states (PDOS) plot for TiN shows that the Fermi level is dominated by the 3d atomic orbitals of Ti, confirming pure TiN's metallicity. The valence bands of TiN_xO_y structures were dominated by 2p orbitals of O at lower energy levels, but they were dominated by 2p orbitals of N at energies close to the valence band maximum (VBM). The conduction bands were dominated by the 3d atomic orbitals of Ti, with the bandgap increasing with O composition leading to creation of shallow trap states near the VBM, which negatively impacts carrier mobility. In conclusion, the on-lattice sampling approach is an effective tool to generate highly crystalline structures of large unit cells, also keeping O substitution for N below 33 % as seen in Ti_2N_2O is crucial for avoiding shallow traps in TiN_xO_y structures.

1. Introduction

The structural diversity of Transition Metal OxyNitride (TMON) materials, which are mostly made up of transition metals and ionic-covalent nitrides, influences both their chemical and physical characteristics. The optical properties, mechanical strength, thermal capabilities, and chemical stability of these materials make them valuable in a variety of industries, including photovoltaic, photothermal, photocatalytic, pigment, lighting, display, optoelectronic, and military. The optical characteristics, which are closely related to the electronic band structure, may be impacted by modifications to the chemical composition and synthesis conditions [1]. Lately, titanium oxynitride, or TiN_xO_y, has garnered more and more interest [2,3]. The films' N/O ratio dictates the material properties of TiN_xO_y films. Low oxygen content TiN_xO_y films have been studied for use as transparent infrared window electrodes, water-resistant and aesthetically pleasing coatings, energy-efficient windows, and fuel cell membrane components. Resistors, insulators, photocatalysts, and dye-solar cells have all been made from high oxygen-content TiN_xO_y materials [4,5].

In this work, various computational approaches to model and simulate realistic TiN_xO_y structures of different stoichiometry were examined. To model meaningful structures, certain questions must be answered such as: Is the knowledge of material chemistry of the structure known? Is there any experimental knowledge that can be leveraged upon? Does the material model structurally agree with the experiment? Is the material model energetically meaningful? How consistent are the

* Corresponding author.
E-mail address: jschall@ncat.edu (J. David Schall).

https://doi.org/10.1016/j.commatsci.2024.113292
Received 1 July 2024; Received in revised form 9 August 2024; Accepted 11 August 2024
Available online 14 August 2024

properties of structural models with experimental results, and can any relationship be drawn between both? By changing the stoichiometry, TiN can be changed from the metallic to the semiconducting TiN_xO_y state [6], thereby creating the potential to develop films with tunable electronic properties, a step that is critical in application to real-world devices. The properties of TiN_xO_y are dependent on the base materials and structure generation methods, such as choosing preferential doping sites for N doping sites of TiO_2 [7,8], corundum Ti_2O_3 [9,10], kinetically limited minimization [11] etc. Research done by Khalil *et al.* [12] modeled TiN_xO_y structure using a TiO_2 basis, they emphasized that the bandgap decreased by substitutional doping with N, however, their band structures and density of states (DOS) plots show presence of electronic states at the Fermi level indicating metallic character. Experimental works cited by Xiao *et al.* [13] show that the lattice parameter of TiN_xO_y reduces with increase in oxygen content in the film, however, their computational work showed otherwise, and charge neutrality was not factored in their computational models of $Ti_4O_2N_2$ and $Ti_{15}O_8N_7$. In addition, their structure turned out to be metallic. Both works [12,13] contrast with the semiconducting characteristics of TiN_xO_y reported by Roy *et al.* [14] and Suvorova *et al.* [15]. Mehmood *et al.* [16] studied the electronic structure and dielectric properties of bulk TiN and surfaces for plasmonic applications. They showed that bulk TiN is metallic. The work presented in this manuscript takes a different approach to observing these assertions. From an experimental standpoint, the synthesis of TiN_xO_y via oxidation has an energetic advantage over the traditional method of bandgap engineering of TiO_2 via nitridation. The oxidation process has a lower activation energy (400 kCal/mole) relative to the nitridation process (570 kCal/mole). Furthermore, due of the lack of an isostructural phase between TiN and TiO_2, it has not been possible to achieve substitutional nitrogen doping above 5.5 atomic percent while nitriding TiO_2 [4,5,14].

Our work intends to compute the electronic band structure as a basis for future research in tailored plasmonic and optical response in TiN_xO_y materials. Ultimately, the goal here is to develop an approach to model these structures and observe the electronic properties of TiN_xO_y by virtue of N/O composition of the structural models. In what follows, we will describe a novel on-site lattice substitution method for structure generation, subsequent calculations of the band gap, and electronic density of states for these structures.

2. Methodology

2.1. Structure modeling

Ascertaining the correct electronic charge for the constituent elements (i.e. Ti, N, and O) is vital to modeling structures. N and O atoms have oxidation states of −3 and −2 respectively, hence the need to determine the oxidation state of Ti in TiN_xO_y as Ti can either be bivalent, trivalent, or tetravalent. Foo *et al*[17] have noted that assigning a charge of +4 to Ti in TiN_xO_y systems gives a better goodness of fit than +3. This finding was corroborated by TiN_xO_y systems on Materials Project [18]. Here, three TiN_xO_y systems with different oxygen compositions (i.e., replacing 33, 50, and 67 % nitrogen with oxygen) were modeled, these compositions were chosen for quantitative reasons to model structures that are lightly, moderately, and highly oxidized.

From the compositions the formula for each charge-balanced composition was determined; this was calculated to be Ti_2N_2O, $Ti_5N_4O_4$, and $Ti_7N_4O_8$ for 33, 50, and 67 % O doping *(see* Supplemental Information *Note S2 for stoichiometry determination)*. Three different methods were used to generate the structures: Cluster Approach to Statistical Mechanics (CASM) [19], Ab initio random structure searching (AIRSS) [20,21], and a novel on-lattice sampling approach. CASM attempts to build all possible permutations of the structure being studied. This becomes a problem when the number of formula units is increased. The number of possible permutations may be on the order of millions which is computationally unfeasible., Due to this limitation the CASM method was abandoned. AIRSS works by iteratively setting the minimum distance between the constituent atoms, and the number of formula units considered. This in turn generates random sensible structures. High energy structures can be eliminated to trim down the number of likely structures based on their space groups and other relevant parameters.

The required formula units for the 33, 50, and 67 % substitutions were obtained by iteratively increasing the number of formula units in the crystal structure and simultaneously observing the energy of the system and the band structure. If too many high energy structures are present within a formula unit, the next one is screened. The required formula units for the 33, 50, and 67 % substitutions were determined to be 8, 3, and 2 respectively, yielding a formula of Ti_2N_2O (40 atoms), $Ti_5N_4O_4$ (39 atoms), and $Ti_7N_4O_8$ (38 atoms) for the 3 structures. This indicates a reduction in cell volume as oxygen content increases a similar trend was observed in experiments [13]. Roy *et al* have attributed this lattice expansion with increased O content to the presence of electrostatic ionic repulsion between O and N in the vicinity of Ti vacancies [14]. Leveraging on prior experimental knowledge [22], we expect that TiN-based TiN_xO_y, which has the cubic rock salt structure, undergoes a change in crystal structure as O substituted onto N lattice sites. From AIRSS sampling, the triclinic P1 space group populated the structure output as compared to other space groups suggesting that the structure of interest belongs to the triclinic group. However, since the reported experimental lattice parameters measured via x-ray diffraction [13] are singular values, the P1 space group was screened for quasi-cubic structures having approximately equal lattice edge lengths for the a, b, and c axis.

Upon simulating the bandgap of the structures using the Kohn-Sham Density Functional Theory (KS-DFT) scheme, the bandgap was observed to increase with O content. The shape of the bands prompted us to examine the relaxed structures as generated by AIRSS. We observed that the structures were amorphous and lacked symmetry because the probability of sampling amorphous phases increases with the number of atoms in the unit cell *(see* Supplemental Information *Fig. S1 and Fig. S2)*. Although these conditions are not critical for bandgap calculations as the trend of the bandgap values followed experimental results [15], they are worth considering for transport properties. To address these concerns, an on-lattice sampling approach was employed. A general flow chart for this approach is given in Fig. 1.

The on-site method starts by identifying a highly crystalline structure of the material of interest, preferably the one with the highest number of atoms. The next step is to export the crystallographic information file into a format readable by the electronic structure simulation code (in this case Quantum ESPRESSO) and parsing it into a Python™ script that randomly removes and substitutes target atomic species (in this case Ti and N) to ensure the output structures are of a pre-determined charge neutral composition. A similarity threshold is imposed to ensure that overly similar structures are not generated. Each structure is then the subject of a variable cell relaxation (vc-relax) scheme that terminates after the first self-consistent field (scf) cycle using an Ultra-Soft Pseudo Potential (USPP) type pseudo potential of Perdew-Burke-Ernzerhof revised for solids (PBEsol) with the Brillouin zone integrated on a 4x4x4 k-point grid sampled using the Monkhorst Pack method. Gaussian smearing was used for this step. As described in more detail below, all the structures have the same basis and can be sorted by energy after the first scf step to screen out unrealistic high energy structures. For further screening purposes, the structures are treated as metallic using the Marzari-Vanderbilt smearing [23] so that a Fermi level can be identified for semiconductors and insulators. Structures having bands crossing the Fermi level are discarded, in our case, there are none. Finally, the structure having the largest bandgap with bands that are not excessively flat is the structure of interest. The Python™ scripts for the on-lattice sampling of $Ti_5N_4O_4$, and $Ti_7N_4O_8$ are provided in the Supplemental Information *notes S5 and S6*.

Structural information obtained from AIRSS such as the number of

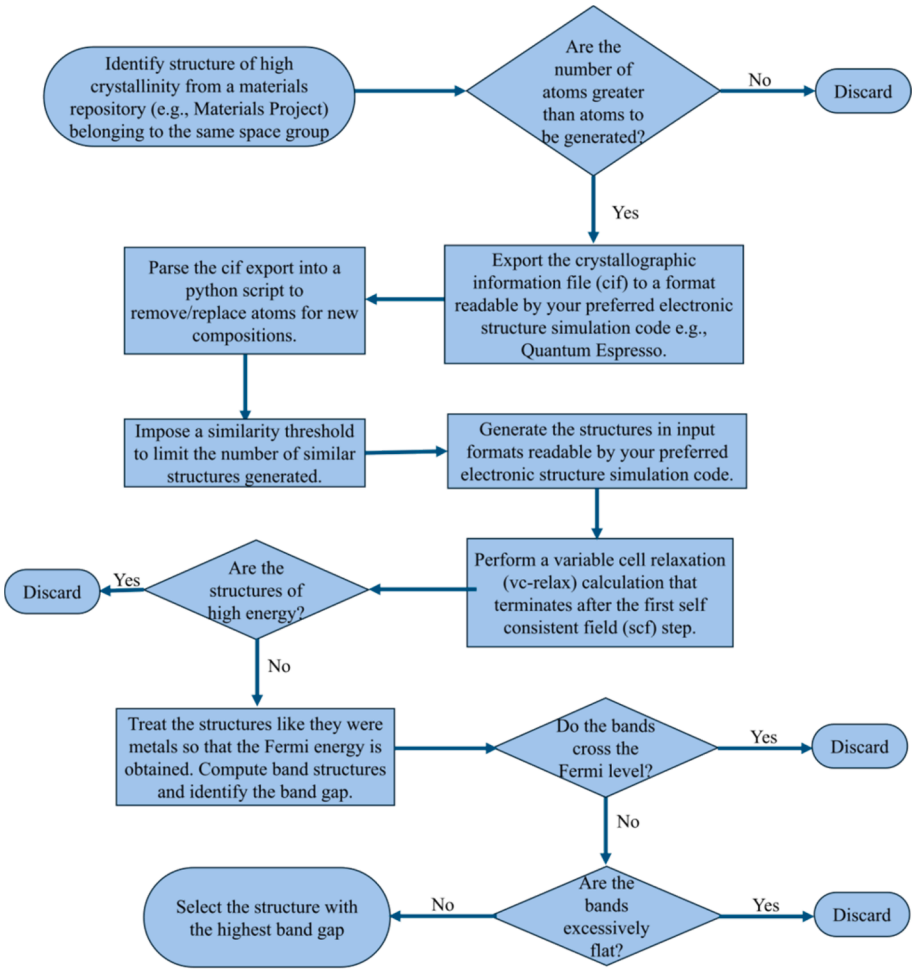

Fig. 1. Flow chart showing the procedures for generating highly crystalline $Ti_5N_4O_4$, and $Ti_7N_4O_8$ structures using the on-lattice sampling approach.

each respective atoms for Ti_2N_2O, $Ti_5N_4O_4$, and $Ti_7N_4O_8$ structures, and the triclinic P1 space group can be leveraged upon. A highly crystalline structure from repositories like Materials Project that use machine learning approaches to model crystalline structures can be used as base structure for on-lattice sampling. This process involves using highly crystalline triclinic P1 space group Ti_2N_2O (mp-775829) [24] from Materials Project as the base structure, replacing the right amount of N atoms for O, and removing the appropriate amount of Ti atoms to achieve the charge neutral compositions of $Ti_5N_4O_4$ and $Ti_7N_4O_8$ respectively just as in AIRSS. This is a randomized combinatorial problem as Ti_2N_2O cell contains 16 Ti atoms, 16 N atoms, and 8 O atoms; $Ti_5N_4O_4$ cell contains 15 Ti atoms, 12 N atoms, and 12 O atoms; $Ti_7N_4O_8$ cell contains 14 Ti atoms, 8 N atoms, and 16 O atoms. Hence, there are 29,120 ways of randomly selecting 1 Ti and 4 N atoms for $Ti_5N_4O_4$; and 1,544,400 ways of randomly selecting 2 Ti and 8 N atoms $Ti_7N_4O_8$. However, it is practically impossible to run bandgap calculations for all the structures, therefore a similarity threshold of 5 % and 10 % was imposed on the $Ti_5N_4O_4$ and $Ti_7N_4O_8$ structures respectively; this brought down the number of structures to 1820 for $Ti_5N_4O_4$ and 4034 for $Ti_7N_4O_8$. The aforementioned Python™ script was written for this procedure. Table 1 below offers clarity for this statement.

Running bands calculations for 5854 structures to identify high and low energy structures is still an expensive task; however, since the structures have the same basis, one can safely predict which structures are useful and which are not from the energies obtained after the first scf cycle of the Kohn-Sham iteration scheme during the vc-relax step. This task was performed on all the structures. The structures were then sorted by energy. All but the twenty lowest energy structures were discarded at this step. Full vc-relax, scf, bands calculations were performed.

Table 1
Composition, combinations, similarity threshold, and number of structures generated for Ti_2N_2O, $Ti_5N_4O_4$, and $Ti_7N_4O_8$.

Structure	Atomic composition			Number of combinations	Similarity threshold imposed	Number of generated structures
	Ti	N	O			
Ti_2N_2O	16	16	8	Base	Base	Base
$Ti_5N_4O_4$	15	12	12	29,120	5 %	1820
$Ti_7N_4O_8$	14	8	16	1,544,400	10 %	4034

Using an ultrasoft PBEsol pseudopotential, and the Brillouin zone integrated on a 4x4x4 k-point grid sampled using the Monkhorst Pack method with the Marzari-Vanderbilt smearing on these twenty structures with the lowest energies for the $Ti_5N_4O_4$ and $Ti_7N_4O_8$ structures, the structure with the highest bandgap was chosen as the material of interest *(see Supplemental Information Fig. S4 and Fig. S5)*. The Figs. 2 and 3 below show the resulting crystalline structures and diffraction patterns for the Ti_2N_2O, $Ti_5N_4O_4$, and $Ti_7N_4O_8$ structures using Visualisation for Electronic Structural Analysis (VESTA) [25]. The structures can be thought of as supercells built upon a TiN lattice, hence their lattice parameters when relaxed are reported in Table 2.

2.2. Electronic property calculations

The accuracy of electronic properties estimation methods is critical in choosing the potential applications of a material, careful

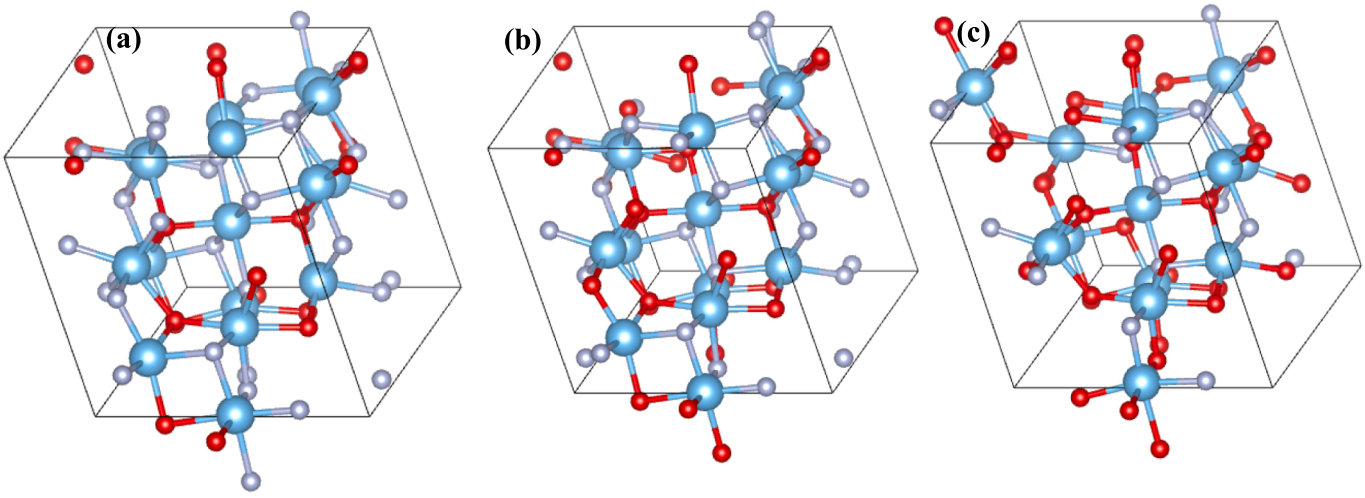

Fig. 2. Crystalline structures for the relaxed (a) Ti_2N_2O, (b) $Ti_5N_4O_4$, and (c) $Ti_7N_4O_8$ structures generated by on-lattice sampling approach.

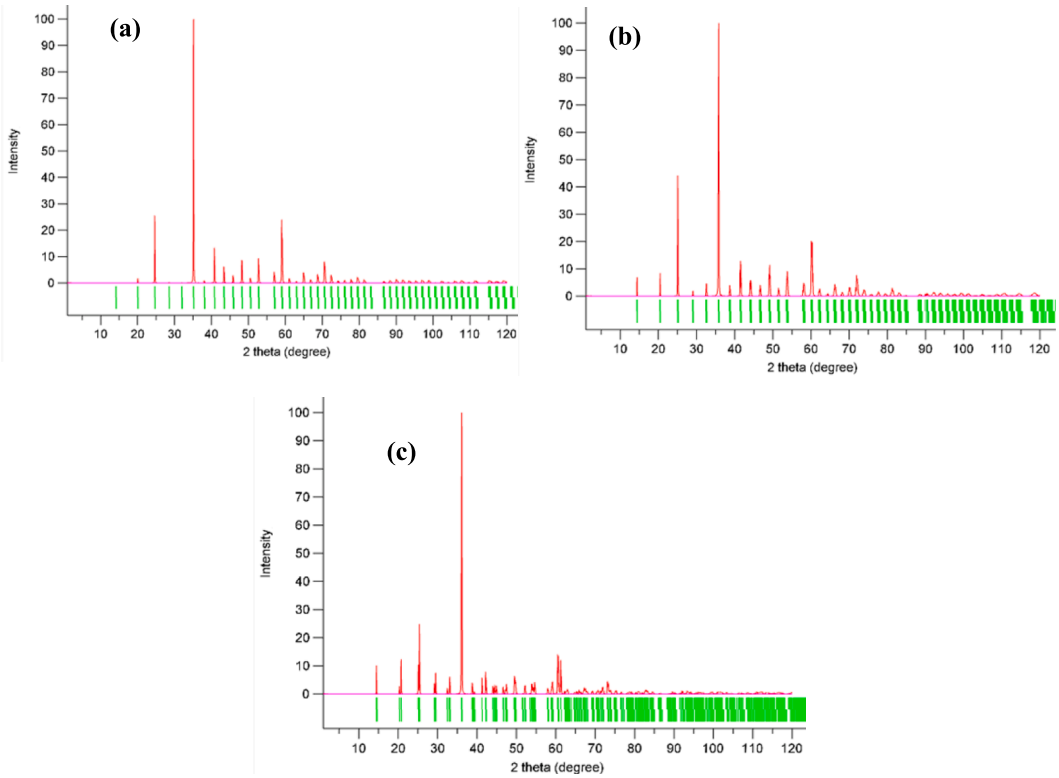

Fig. 3. Diffraction patterns of the crystalline (a) Ti_2N_2O, (b) $Ti_5N_4O_4$, and (c) $Ti_7N_4O_8$ structures generated by on-lattice sampling approach.

Table 2
Structural parameters of relaxed crystalline Ti_2N_2O, $Ti_5N_4O_4$, and $Ti_7N_4O_8$.

Structure	Lattice parameter (Å)	Angles (°)
Ti_2N_2O	7.65	$\alpha = 109.47, \beta = 109.53, \gamma = 109.34$
$Ti_5N_4O_4$	7.52	$\alpha = 109.19, \beta = 109.39, \gamma = 109.65$
$Ti_7N_4O_8$	7.46	$\alpha = 110.01, \beta = 110.24, \gamma = 108.27$

consideration ought to be given to the effectiveness of a chosen approach, ease of computing relevant parameters, and cost of production run. In the subsequent headings, detailed explanations of the tools and approaches followed are given.

2.2.1. *The Exchange-Correlation energy functional*

Local, and semi-local functionals such as LDA, GGA, and *meta*-GGA approximations contain spurious electron self-interaction energy, leading to substantial inaccuracies in reaction energies and gross underestimation of energy gaps between occupied and unoccupied states in solids due to derivative discontinuities and delocalization error [26–30]. To address this, methods like the Hubbard U parameter can be used. The Hubbard U method cancels some of the self-interaction energy on orbitals, like localized d- or f-orbitals. Methods including time-dependent DFT, excited-state techniques like GW [31,32], and the hybrid HSE functional have been developed to address these issues [33–36]. These approaches are more computationally demanding but can yield more accurate predictions of electronic structures. For band gap correction, Koopmans functionals offer an accurate and less expensive approach.

The Koopmans approach has been used to study the properties of Si and ZnO crystals and compared to other approaches like G_0W_0 [37] (which uses the Green's function and the screened Coulomb interaction) and experimental values [38]; the Koopmans values for the bandgaps were 1.16 eV and 3.35 eV for Si and ZnO respectively, while the G_0W_0 values for the same are 1.06 eV and 1.96 eV. For these materials, the experimental bandgaps were 1.17 eV and 3.44 eV for Si and ZnO respectively, hence Koopmans functionals offer an excellent justification for both computational cost and accuracy.

2.2.2. Koopmans Theory/Functional

According to Koopmans' theorem, the first ionization energy of a molecule is equal to the negative of the energy of the highest occupied molecular orbital (HOMO). Koopmans' theorem is a technique that approximates orbital energy ε_i, which is generated from spin orbital wavefunction and kinetic and nuclear attraction energies, using the Hartree-Fock method. This is applicable when a positive ion is created by removing an electron from a molecular orbital [39].

The accuracy and effectiveness of Kohn-Sham density functional theory (KS-DFT) make electronic structure simulations highly influential in many scientific domains. Nonetheless, precise KS-DFT is limited to describing a system's total energy. Complex methods, frequently based on Green's function theory, are needed to achieve accurate first-principles predictions of bandgaps, photo-emission spectra, and band structures [40,41]. To bridge the gap between Green's function theory and KS-DFT, Koopmans-compliant (KC) functionals have been developed. Through the imposition of physically motivated conditions to approximate density functionals, KC functionals preserve the benefits of a functional formulation. The whole manifold is extended to the generalized piecewise linearity (PWL) of the total energy as a function of the total number of electrons or occupation of the highest occupied orbital (HOMO). This results in orbital-density-dependent functionals that are beyond-DFT and sufficiently flexible to accurately describe both ground states and charged excitations. The localization of the "variational" orbitals, which minimize the KC energy, and the accurate description of screening and relaxation effects upon the addition or removal of an electron from the system are characteristics of KC functionals. This property is essential for deriving relevant and precise results in periodic or extended systems [42]. To recast the Koopmans corrections as integrals over the Brillouin zone of the primitive cell, the formalism takes advantage of the Wannier-like character of the variational orbitals. This formalism allows for the natural and simple recovery of band structures as well as the implementation of periodic boundaries. The wannier90 code [43] is used to compute the Wannier Functions (WF). By projecting the eigen states onto the atomic orbitals, the WFs for the valence and conduction bands were computed separately, and based on their dominance in the valence and conduction bands, the atomic orbitals are selected. A transparent and effective implementation of Koopmans functionals for periodic systems can be achieved by recasting the evaluation of screened KC corrections into a linear-response problem amenable to an efficient implementation based on density functional perturbation theory [44]. The *Supplementary Information note S1* provides the basic theory for Koopmans Integers.

3. Results and discussion

3.1. Bandgap calculations

3.1.1. Production calculations with Quantum Espresso

Production calculations begin with convergence of kinetic energy cutoff (Ry) for wavefunctions, k-points, and the property of interest, in this case the bandgap. All calculations were performed on the Bridges-2 at Pittsburgh Supercomputing Center using resources provided through the NSF-funded Advanced Cyberinfrastructure Ecosystem: Services and Support (ACCESS) [45]. The following tasks involve comparing the properties of TiN (mp-492) [46], Ti_2N_2O (mp-775829) [24], $Ti_5N_4O_4$, and $Ti_7N_4O_8$ using scalar-relativistic ONCVPSP (Optimized Norm-Conserving Vanderbilt PSeudoPotential). The Quantum ESPRESSO [47–49] package's plane-wave self-consistent field (PWSCF) method was employed for these calculations. A 12x12x12 k-point grid sampling using the Monkhorst Pack method was used for the Brillouin zone integration for standard KS-DFT calculations. For the pure TiN structure, Maximally Localized Wannier Functions (MLWF) [50] were utilized by projecting the eigen states onto the sp^3 and d orbitals of Ti, and s, and p orbitals of N for band structure correction showing zero bandgap as seen in Fig. 4a below. This projection was performed on an 8x8x8 grid as denser k-point meshes produced distorted band structures. The zero mark indicates the position of the Fermi energy and the band path is corrected for the eigenmode with the highest energy at wavevector L. The Ti_2N_2O, $Ti_5N_4O_4$, and $Ti_7N_4O_8$ structures had direct bandgaps of 1.03 eV, 1.21 eV, and 1.74 eV respectively. Here the zero mark indicates the valence band maximum (VBM). The bands at the Γ point are degenerate for the TiN and there are 2 degenerate bands at the Γ point for the Ti_2N_2O band structure, this degeneracy reduces with increase in O composition.

The Koopmans corrections were computed using the *kcw.x* implementation on Quantum ESPRESSO on 4x4x4 k and q grids. The Wannier Functions (WF) were computed by projecting the eigen states onto the atomic orbitals and hybrids. For the valence bands, the projections chosen were sp^3 and sp^2 for the N atoms, and sp^3 and sp for the O atoms; while for the conduction bands, the projection chosen was d for the Ti atoms for the TiN_xO_y systems. An increase in bandgap with oxygen content was observed with increasing O doping (Fig. 4b, 4c, and 4d) which is in full agreement with experimental results; this is observed with an upward shift of the conduction band. The bandgap values obtained for Ti_2N_2O, $Ti_5N_4O_4$, and $Ti_7N_4O_8$ are 2.68 eV (this is comparable to the 2.62 eV value of corundum-based Ti_2N_2O obtained from GW [9]), 3.03 eV, and 3.65 eV respectively. This implies that during a de-excitation process, Ti_2N_2O will emit blue light, $Ti_5N_4O_4$ will emit violet, and $Ti_7N_4O_8$ is transparent to visible light.

The lifting of the degeneracy when oxygen is incorporated into the rocksalt TiN material caused a break in the symmetry of its crystal structure, which led to the splitting of degenerate bands. This is visible as the material transitioned from rocksalt TiN to a quasi-cubic triclinic P1 structure as observed by changes in the lattice dimensions and the band structure especially at the Γ – point. This reduction of degenerate bands causes TiN_xO_y to absorb light at shorter wavelengths (higher energies), leading to a blue shift in the absorption edge. Higher carrier mobility can often be possible in degenerate bands because multiple states at the same energy level are available for electron conduction in the case of TiN. The effective mass of carriers might increase as a result of these bands splitting, which would lower carrier mobility and, in turn, electrical conductivity. The carrier effective mass of electrons was observed to increase with O composition along R- Γ –T as seen in Table 3.

Table 3 below shows the KS-DFT and Koopmans computed effective masses of holes and electrons of TiN_xO_y at the Γ point. The values obtained are consistent with each other as evidenced by quality interpolation of band structures. The carrier effective mass of electrons was observed to increase with O composition, while that of holes reduced along R- Γ –T. Furthermore, the heavy hole masses might be a concern for material exploitation in real devices as the holes might be problematic to extract from the bulk material to the surface where reactions occur as heavy holes are usually found in oxides and nitrides semiconductors [51], although co-doping might help alleviate some of these issues. Nonetheless, these structures are useful in photoactivated processes as the intrinsic electric field might facilitate the charges diffusion, potentially delaying the recombination process. The carrier effective masses were computed using the expression [52],$m^* = \hbar^2(\frac{d^2E}{dk^2})^{-1}$

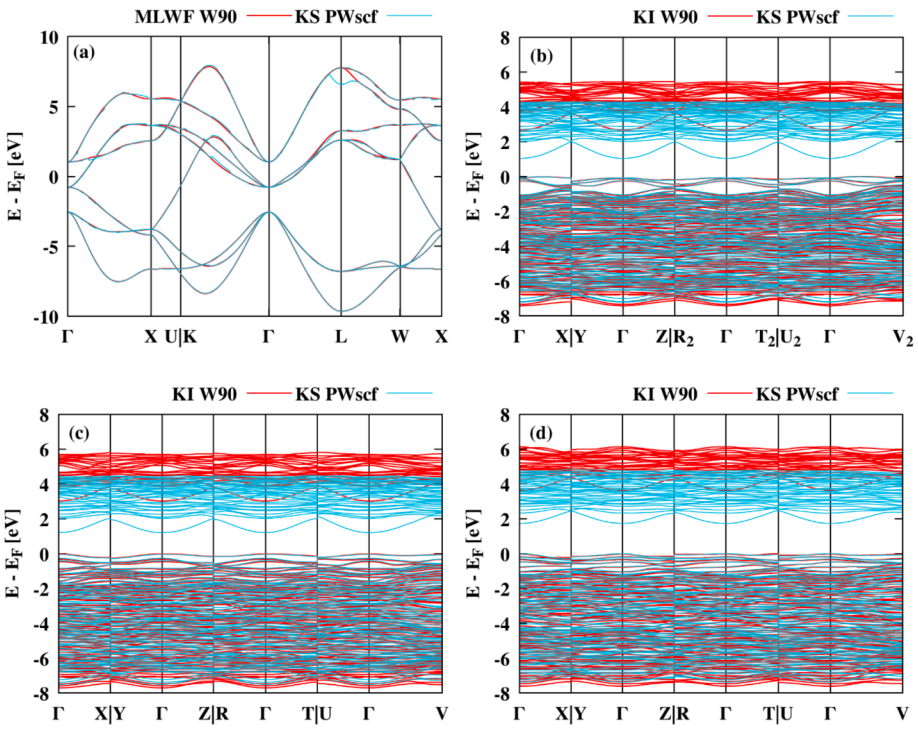

Fig. 4. Electronic band diagrams for (a) TiN, (b) Ti_2N_2O, and on-lattice sampling-generated (c) $Ti_5N_4O_4$, and (d) $Ti_7N_4O_8$ structures.

Table 3
Carrier effective masses of Ti_2N_2O, $Ti_5N_4O_4$, and $Ti_7N_4O_8$ at the Γ point.

Structure	Band path	KS-DFT			Koopmans		
		m_h (m_0)	m_e (m_0)	Bandgap (eV)	m_h (m_0)	m_e (m_0)	Bandgap (eV)
Ti_2N_2O	Y- Γ −Z	3.055	0.838	1.03	3.893	0.823	2.68
	R_2- Γ −T_2	5.847	0.814		8.053	0.845	
	U_2- Γ −V_2	3.278	0.986		3.763	0.875	
$Ti_5N_4O_4$	Y- Γ −Z	3.462	0.971	1.21	3.706	1.024	3.03
	R- Γ −T	4.551	0.902		4.341	0.957	
	U- Γ −V	3.280	0.961		3.959	1.075	
$Ti_7N_4O_8$	Y- Γ −Z	1.898	0.573	1.74	2.431	0.590	3.65
	R- Γ −T	3.085	1.130		3.774	1.133	
	U- Γ −V	2.212	1.236		3.225	1.044	

3.2. Density of states (DOS) and projected density of states (PDOS) of TiN and TiN_xO_y

The PDOS plot for TiN as seen in Fig. 5a shows that the Fermi level (zero mark of the plot) is dominated by the 3d atomic orbitals of Ti; this further proves that pure TiN is metallic, and it corroborates the band structure of TiN; this calculation was performed using a non-scf kpoint grid of 60x60x60. The valence bands of the TiN_xO_y structures are dominated by the 2p orbitals of O at lower energy levels, however they are dominated by 2p orbitals of N at energies close to the VBM. Conversely, the conduction bands are dominated by the 3d atomic orbitals of Ti, with the bandgap increasing as O composition increases and holding same values as calculated from the band structure as seen in Fig. 5b, 5c, and 5d. Furthermore, it is observed that the increase in O composition in the TiN_xO_y structures beyond 33 % leads to creation of shallow trap states near the VBM; these shallow trap states greatly reduce carrier mobility.

The shallow traps can act as scattering centers, hindering carrier transport and reducing carrier mobility; for device applications, this can result in reduced device performance and slower operation speeds. Carriers captured by a shallow trap are momentarily immobilized within the trap and prevent it from participating in the carrier transport process. However, in certain cases, the trapped carrier can be released or detrapped, regain its mobility and participate in carrier transport. The energy level of a shallow trap also plays a significant role in its impact on carrier mobility. Shallow traps closer to band edges like those discussed here have a higher probability of capturing carriers due to their more energetic accessibility. From our structures, it can be determined that keeping N substitution for O below 33 % is important for avoiding creation of shallow traps.

4. Conclusion

The on-lattice sampling approach offers a top-down approach to model new crystalline structures of large unit cells. This approach is advantageous if the space group and number of atoms in the new structure are known, e.g., via experimental measurement. The on-site sampling method is used make up for deficiencies of CASM and AIRSS. This approach was used to generate highly crystalline $Ti_5N_4O_4$ and $Ti_7N_4O_8$ (50 % and 67 % N replacement by O) built from a highly crystalline Ti_2N_2O basis (33 % N replacement by O) (mp-775829) [24] from Materials Project. Both the KS-DFT scheme and Koopmans integers were utilized for band structure calculation. The Ti_2N_2O, $Ti_5N_4O_4$, and $Ti_7N_4O_8$ structures had direct bandgaps of 1.03 eV, 1.21 eV, and 1.74 eV

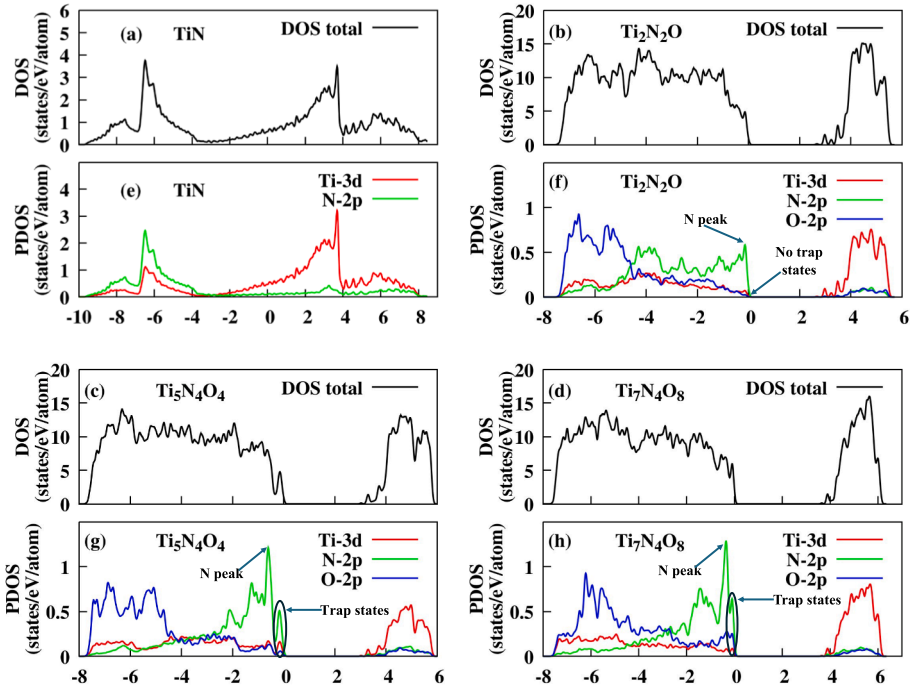

Fig. 5. DOS (a-d) and PDOS (e-h) plots for TiN, Ti_2N_2O, $Ti_5N_4O_4$, and $Ti_7N_4O_8$ structures.

respectively according to KS-DFT; Koopmans functionals offer an accurate and less expensive approach for bandgap correction with values of 2.68 eV, 3.03 eV, and 3.65 eV respectively for the same structures. The carrier effective mass of electrons along R- Γ –T was observed to increase with O composition, while that of holes reduced. The PDOS plot for TiN shows that the Fermi level is dominated by the 3d atomic orbitals of Ti proving that pure TiN is metallic; the valence bands of the TiN_xO_y structures were dominated by the 2p orbitals of O at lower energy levels, however they are dominated by 2p orbitals of N at energies close to the VBM. Conversely, the conduction bands are dominated by the 3d atomic orbitals of Ti, with the bandgap holding same values as calculated from the band structure. Furthermore, the increase in O composition in the TiN_xO_y structures led to creation of shallow trap states near the VBM; these shallow trap states greatly impact carrier mobility. Shallow traps closer to band edges like those observed have a higher probability of capturing carriers due to their more energetic accessibility; and keeping N substitution for O at or below 33 % is important for avoiding creation of shallow traps.

CRediT authorship contribution statement

Abiodun A. Odusanya: . **Dhananjay Kumar:** Funding acquisition. **J. David Schall:** Writing – review & editing, Validation, Supervision, Project administration. **Justin Mayer:** Supervision, Conceptualization. **Ridwan Sakidja:** Methodology.

Declaration of competing interest

The authors declare that they have no known competing financial interests or personal relationships that could have appeared to influence the work reported in this paper.

Data availability

Data will be made available on request.

Acknowledgments

The authors would like to acknowledge the financial support from the National Science Foundation, NSF-PREM, via grant number DMR-2122067. This work used Bridges-2 at Pittsburgh Supercomputing Center through allocation MAT220024 from the Advanced Cyberinfrastructure Coordination Ecosystem: Services & Support (ACCESS) program, which is supported by National Science Foundation grants #2138259, #2138286, #2138307, #2137603, and #2138296.

Data availability statement

The raw data required to reproduce these findings are available by request.

Appendix A. Supplementary data

Supplementary data to this article can be found online at https://doi.org/10.1016/j.commatsci.2024.113292.

References

[1] R.J. Xie, H.T. Hintzen, Optical properties of (oxy)nitride materials: A review, Journal of the American Ceramic Society 96 (2013) 665–687, https://doi.org/10.1111/jace.12197.
[2] Y. Zheng, P. Wu, H. Yang, Z. Yi, Y. Luo, L. Liu, Q. Song, M. Pan, J. Zhang, P. Cai, High efficiency Titanium oxides and nitrides ultra-broadband solar energy absorber and thermal emitter from 200 nm to 2600 nm, Opt Laser Technol 150 (2022), https://doi.org/10.1016/j.optlastec.2022.108002.
[3] R. Mishra, C.W. Chang, A. Dubey, Z.Y. Chiao, T.J. Yen, H.W. Howard Lee, Y.J. Lu, S. Gwo, Optimized Titanium Nitride Epitaxial Film for Refractory Plasmonics and Solar Energy Harvesting, Journal of Physical Chemistry C 125 (2021) 13658–13665. DOi: 10.1021/acs.jpcc.1c03053.
[4] I. Seki, Kinetic investigation into the formation of titanium nitride from titanium dioxide by carbonitrization, Mater Trans 58 (2017) 1546–1554, https://doi.org/10.2320/matertrans.MAW201711.
[5] H.-Y. Chen, F.-H. Lu, Oxidation behavior of titanium nitride films, Journal of Vacuum Science & Technology a: Vacuum, Surfaces, and Films 23 (2005) 1006–1009, https://doi.org/10.1116/1.1914815.
[6] N.R. Mucha, J. Som, S. Shaji, S. Fialkova, P.R. Apte, B. Balasubramanian, J. E. Shield, M. Anderson, D. Kumar, Electrical and optical properties of titanium oxynitride thin films, J Mater Sci 55 (2020) 5123–5134, https://doi.org/10.1007/s10853-019-04278-x.
[7] C. Di Valentin, E. Finazzi, G. Pacchioni, A. Selloni, S. Livraghi, M.C. Paganini, E. Giamello, N-doped TiO2: Theory and experiment, Chem Phys 339 (2007) 44–56, https://doi.org/10.1016/j.chemphys.2007.07.020.

[8] M. Ceotto, L. Lo Presti, G. Cappelletti, D. Meroni, F. Spadavecchia, R. Zecca, M. Leoni, P. Scardi, C.L. Bianchi, S. Ardizzone, About the nitrogen location in nanocrystalline N-doped TiO 2: Combined DFT and EXAFS approach, Journal of Physical Chemistry C 116 (2012) 1764–1771. DOi: 10.1021/jp2097636.

[9] Y. Aoki, M. Sakurai, S. Coh, J.R. Chelikowsky, S.G. Louie, M.L. Cohen, S. Saito, Insulating titanium oxynitride for visible light photocatalysis, Phys Rev B 99 (2019), https://doi.org/10.1103/PhysRevB.99.075203.

[10] L. Allan, G.O. Amolo, J. Mwabora, S. Mureramanzi, The Impact of Nitrogen Doping on Structural and Electronic Properties of Titanium Sesquioxide, An ab-initio Study, 2022.

[11] A. Sharan, S. Lany, Computational discovery of stable and metastable ternary oxynitrides, Journal of Chemical Physics 154 (2021), https://doi.org/10.1063/5.0050356.

[12] M. Khalil, A. Bashir, E.A. Alghamdi, A.A. Siddig, S.M. Ramay, M. Saleem, Study of epsilon-near-zero response in Al substituted titanium oxynitride thin films using computational and experimental investigations, Materials Science and Engineering: B 291 (2023), https://doi.org/10.1016/j.mseb.2023.116369.

[13] J. Xiao, B. Jiang, K. Huang, H. Zhu, Structural and elastic properties of TiCxN1-x, TiCxO1-x, TiOxN 1–x solid solutions from first-principles calculations, Comput Mater Sci 88 (2014) 86–91, https://doi.org/10.1016/j.commatsci.2014.02.042.

[14] M. Roy, K. Sarkar, J. Som, M.A. Pfeifer, V. Craciun, J.D. Schall, S. Aravamudhan, F. W. Wise, D. Kumar, Modulation of Structural, Electronic, and Optical Properties of Titanium Nitride Thin Films by Regulated In Situ Oxidation, ACS Appl Mater Interfaces 15 (2023) 4733–4742, https://doi.org/10.1021/acsami.2c18926.

[15] E.I. Suvorova, O.V. Uvarov, K.V. Chizh, A.A. Klimenko, P.A. Buffat, Structure, Oxygen Content and Electric Properties of Titanium Nitride Electrodes in TiNx/La: HfO2/TiNx Stacks Grown by PEALD on SiO2/Si, Nanomaterials 12 (2022), https://doi.org/10.3390/nano12203608.

[16] F. Mehmood, R. Pachter, N.R. Murphy, W.E. Johnson, Electronic and optical properties of titanium nitride bulk and surfaces from first principles calculations, J Appl Phys 118 (2015), https://doi.org/10.1063/1.4935813.

[17] C. Foo, Y. Li, K. Lebedev, T. Chen, S. Day, C. Tang, S.C.E. Tsang, Characterisation of oxygen defects and nitrogen impurities in TiO2 photocatalysts using variable-temperature X-ray powder diffraction, Nat Commun 12 (2021), https://doi.org/10.1038/s41467-021-20977-z.

[18] A. Jain, S.P. Ong, G. Hautier, W. Chen, W.D. Richards, S. Dacek, S. Cholia, D. Gunter, D. Skinner, G. Ceder, K.A. Persson, Commentary: The materials project: A materials genome approach to accelerating materials innovation, APL Mater 1 (2013), https://doi.org/10.1063/1.4812323.

[19] B. Puchala, J.C. Thomas, A.R. Natarajan, J.G. Goiri, S.S. Behara, J.L. Kaufman, A. Van der Ven, CASM — A software package for first-principles based study of multicomponent crystalline solids, Comput Mater Sci 217 (2023), https://doi.org/10.1016/j.commatsci.2022.111897.

[20] C.J. Pickard, R.J. Needs, Ab initio random structure searching, Journal of Physics Condensed Matter 23 (2011), https://doi.org/10.1088/0953-8984/23/5/053201.

[21] C.J. Pickard, R.J. Needs, High-pressure phases of silane, Phys Rev Lett 97 (2006), https://doi.org/10.1103/PhysRevLett.97.045504.

[22] V.V. Buranych, A.D. Pogrebnjak, M. Pogorielov, K. Diedkova, D. Aubakirova, I. Savitskaya, A.I. Kupchishin, N. Kulenova, Characterization, mechanical and biomedical properties of titanium oxynitride coating, Ceram Int 49 (2023) 28167–28174, https://doi.org/10.1016/j.ceramint.2023.06.070.

[23] N. Marzari, D. Vanderbilt, A. De Vita, M.C. Payne, Thermal Contraction and Disordering of the Al(110) Surface, Phys. Rev. Lett. 82 (1999) 3296–3299, https://doi.org/10.1103/PhysRevLett.82.3296.

[24] Materials Project v2023.11.1. (2023). https://next-gen.materialsproject.org/materials/mp-775829.

[25] K. Momma, F. Izumi, *VESTA 3* for three-dimensional visualization of crystal, volumetric and morphology data, J Appl Crystallogr 44 (2011) 1272–1276, https://doi.org/10.1107/S0021889811038970.

[26] N.E. Kirchner-Hall, W. Zhao, Y. Xiong, I. Timrov, I. Dabo, Extensive benchmarking of DFT+U calculations for predicting band gaps, Applied Sciences (switzerland) 11 (2021), https://doi.org/10.3390/app11052395.

[27] A. Bajaj, H.J. Kulik, Molecular DFT+U: A Transferable, Low-Cost Approach to Eliminate Delocalization Error, Journal of Physical Chemistry Letters 12 (2021) 3633–3640, https://doi.org/10.1021/acs.jpclett.1c00796.

[28] S.A. Tolba, K.M. Gameel, B.A. Ali, H.A. Almossalami, N.K. Allam, The DFT+U: Approaches, Accuracy, and Applications, in: Density Functional Calculations - Recent Progresses of Theory and Application, InTech, 2018. DOi: 10.5772/intechopen.72020.

[29] B. Himmetoglu, A. Floris, S. De Gironcoli, M. Cococcioni, Hubbard-corrected DFT energy functionals: The LDA+U description of correlated systems, Int J Quantum Chem 114 (2014) 14–49, https://doi.org/10.1002/qua.24521.

[30] I. Timrov, N. Marzari, M. Cococcioni, HP – A code for the calculation of Hubbard parameters using density-functional perturbation theory, (2022). DOi: 10.1016/j.cpc.2022.108455.

[31] M.J. Van Setten, F. Weigend, F. Evers, The GW-method for quantum chemistry applications: Theory and implementation, J Chem Theory Comput 9 (2013) 232–246, https://doi.org/10.1021/ct300648t.

[32] L. Reining, The GW approximation: content, successes and limitations, Wiley Interdiscip Rev Comput Mol Sci 8 (2018), https://doi.org/10.1002/wcms.1344.

[33] M.A. Flores, W. Orellana, E. Menéndez-Proupin, On the Accuracy of the HSE Hybrid Functional to Describe Many-Electron Interactions and Charge Localization in Semiconductors (2018), https://doi.org/10.1103/PhysRevB.98.155131.

[34] S. Śmiga, L.A. Constantin, Unveiling the Physics behind Hybrid Functionals, Journal of Physical Chemistry A 124 (2020) 5606–5614, https://doi.org/10.1021/acs.jpca.0c04156.

[35] B.G. Janesko, T.M. Henderson, G.E. Scuseria, Screened hybrid density functionals for solid-state chemistry and physics, Physical Chemistry Chemical Physics 11 (2009) 443–454, https://doi.org/10.1039/b812838c.

[36] A.V. Arbuznikov, Hybrid exchange correlation functionals and potentials: Concept elaboration, Journal of Structural Chemistry 48 (2007) S1–S31, https://doi.org/10.1007/s10947-007-0147-0.

[37] T. Rangel, M. Del Ben, D. Varsano, G. Antonius, F. Bruneval, F.H. da Jornada, M. J. van Setten, O.K. Orhan, D.D. O'Regan, A. Canning, A. Ferretti, A. Marini, G. M. Rignanese, J. Deslippe, S.G. Louie, J.B. Neaton, Reproducibility in G0W0 calculations for solids, Comput Phys Commun 255 (2020), https://doi.org/10.1016/j.cpc.2020.107242.

[38] E.B. Linscott, N. Colonna, R. De Gennaro, N.L. Nguyen, G. Borghi, A. Ferretti, I. Dabo, N. Marzari, koopmans: An Open-Source Package for Accurately and Efficiently Predicting Spectral Properties with Koopmans Functionals, J Chem Theory Comput (2023), https://doi.org/10.1021/acs.jctc.3c00652.

[39] J. Luo, Z.Q. Xue, W.M. Liu, J.L. Wu, Z.Q. Yang, Koopmans' Theorem for Large Molecular Systems within Density Functional Theory, J Phys Chem A 110 (2006) 12005–12009, https://doi.org/10.1021/jp063669m.

[40] H. Cao, Z. Yu, P. Lu, L.-W. Wang, Fully converged plane wave based self-consistent GW calculations of periodic solids, n.d.

[41] C. Buth, U. Birkenheuer, M. Albrecht, P. Fulde, Ab initio Green's function formalism for band structures, 2005.

[42] N. Colonna, R. De Gennaro, E. Linscott, N. Marzari, Koopmans Spectral Functionals in Periodic Boundary Conditions, J Chem Theory Comput (2022), https://doi.org/10.1021/acs.jctc.2c00161.

[43] G. Pizzi, V. Vitale, R. Arita, S. Blügel, F. Freimuth, G. Géranton, M. Gibertini, D. Gresch, C. Johnson, T. Koretsune, J. Ibañez-Azpiroz, H. Lee, J.M. Lihm, D. Marchand, A. Marrazzo, Y. Mokrousov, J.I. Mustafa, Y. Nohara, Y. Nomura, L. Paulatto, S. Poncé, T. Ponweiser, J. Qiao, F. Thöle, S.S. Tsirkin, M. Wierzbowska, N. Marzari, D. Vanderbilt, I. Souza, A.A. Mostofi, J.R. Yates, Wannier90 as a community code: New features and applications, Journal of Physics Condensed Matter 32 (2020). DOi: 10.1088/1361-648X/ab51ff.

[44] L.-W. Wang, Band gap corrections for molecules and solids using Koopmans theorem and Wannier functions, 2015. https://www.researchgate.net/publication/273005620.

[45] S.T. Brown, P. Buitrago, E. Hanna, S. Sanielevici, R. Scibek, N.A. Nystrom, Bridges-2: A Platform for Rapidly-Evolving and Data Intensive Research, in: Practice and Experience in Advanced Research Computing, ACM, New York, NY, USA, 2021, pp. 1–4, https://doi.org/10.1145/3437359.3465593.

[46] Materials Project, mp-492: TiN (Cubic, Fm-3m, 225), Materials Project v2023.11.1. (2023). https://next-gen.materialsproject.org/materials/mp-492.

[47] P. Giannozzi, O. Baseggio, P. Bonfà, D. Brunato, R. Car, I. Carnimeo, C. Cavazzoni, S. De Gironcoli, P. Delugas, F. Ferrari Ruffino, A. Ferretti, N. Marzari, I. Timrov, A. Urru, S. Baroni, Quantum ESPRESSO toward the exascale, Journal of Chemical Physics 152 (2020), https://doi.org/10.1063/5.0005082.

[48] P. Giannozzi, S. Baroni, N. Bonini, M. Calandra, R. Car, C. Cavazzoni, D. Ceresoli, G.L. Chiarotti, M. Cococcioni, I. Dabo, A. Dal Corso, S. De Gironcoli, S. Fabris, G. Fratesi, R. Gebauer, U. Gerstmann, C. Gougoussis, A. Kokalj, M. Lazzeri, L. Martin-Samos, N. Marzari, F. Mauri, R. Mazzarello, S. Paolini, A. Pasquarello, L. Paulatto, C. Sbraccia, S. Scandolo, G. Sclauzero, A.P. Seitsonen, A. Smogunov, P. Umari, R.M. Wentzcovitch, QUANTUM ESPRESSO: A modular and open-source software project for quantum simulations of materials, Journal of Physics Condensed Matter 21 (2009), https://doi.org/10.1088/0953-8984/21/39/395502.

[49] P. Giannozzi, O. Andreussi, T. Brumme, O. Bunau, M. Buongiorno Nardelli, M. Calandra, R. Car, C. Cavazzoni, D. Ceresoli, M. Cococcioni, N. Colonna, I. Carnimeo, A. Dal Corso, S. De Gironcoli, P. Delugas, R.A. Distasio, A. Ferretti, A. Floris, G. Fratesi, G. Fugallo, R. Gebauer, U. Gerstmann, F. Giustino, T. Gorni, J. Jia, M. Kawamura, H.Y. Ko, A. Kokalj, E. Küçükbenli, M. Lazzeri, M. Marsili, N. Marzari, F. Mauri, N.L. Nguyen, H.V. Nguyen, A. Otero-De-La-Roza, L. Paulatto, S. Poncé, D. Rocca, R. Sabatini, B. Santra, M. Schlipf, A.P. Seitsonen, A. Smogunov, I. Timrov, T. Thonhauser, P. Umari, N. Vast, X. Wu, S. Baroni, Advanced capabilities for materials modelling with Quantum ESPRESSO, Journal of Physics Condensed Matter 29 (2017), https://doi.org/10.1088/1361-648X/aa8f79.

[50] N. Marzari, A.A. Mostofi, J.R. Yates, I. Souza, D. Vanderbilt, Maximally localized Wannier functions: Theory and applications, Rev Mod Phys 84 (2012) 1419–1475, https://doi.org/10.1103/RevModPhys.84.1419.

[51] M. Palummo, M. Re Fiorentin, K. Yamashita, I.E. Castelli, G. Giorgi, Study of Optoelectronic Features in Polar and Nonpolar Polymorphs of the Oxynitride Tin-Based Semiconductor InSnO2N, Journal of Physical Chemistry Letters 14 (2023) 1548–1555, https://doi.org/10.1021/acs.jpclett.3c00211.

[52] C. Kittel, P. McEuen, Introduction to solid state physics, John Wiley & Sons, 2018.